

A magnetohydrodynamic simulation of pellet ablation in the electrostatic approximation

Roman Samulyak¹, Tianshi Lu¹ and Paul Parks²

¹ Computational Science Center, Brookhaven National Laboratory, Upton, NY 11973, USA

² General Atomics, PO Box 85608, San Diego, CA 92186-5608, USA

Received 16 June 2006, accepted for publication 11 December 2006

Published 10 January 2007

Online at stacks.iop.org/NF/47/103

Abstract

A magnetohydrodynamic numerical model for hydrogenic pellet ablation in the electrostatic approximation has been developed based on the method of front tracking. The main features of the model are the explicit tracking of interfaces that separate the solid pellet from the ablated gas and the cold, dense and weakly ionized ablation cloud from the highly conducting fusion plasma, a surface ablation model, a kinetic model for the electron heat flux and an equation of state accounting for atomic processes in the ablation cloud. The interaction of the pellet ablation flow with the magnetic field including the $\mathbf{J} \times \mathbf{B}$ Lorentz force is studied here systematically for the first time. The model has also been validated through the comparison with the semi-analytic Transonic Flow model and previous purely hydrodynamic simulations. Contrary to prevailing expectations, the ablation rate is reduced only slightly when the geometry is changed from spherically symmetric to axially symmetric, in the case of purely hydrodynamic models. However, in the magnetohydrodynamic simulations the $\mathbf{J} \times \mathbf{B}$ force funnels the flow into an extended plasma shield, which intercepts the incident plasma heat flux and reduces the ablation rate, depending on the rise time of heat flux seen by the pellet. Shorter ‘warm-up’ times lead to narrower ablation channels, stronger shielding and reduced ablation rates. This new feature implies that pellets traversing strong plasma gradients, as in the edge pedestal region of the ITER plasma, could have significantly lower ablation rates if injected at higher velocity.

PACS numbers: 28.52.Cx, 52.65.Kj

(Some figures in this article are in colour only in the electronic version)

1. Introduction

The injection of frozen pellets of deuterium and tritium proposed in [1] is considered the major mechanism for refuelling of nuclear fusion reactors of the tokamak configuration. This problem is significantly important for the International Thermonuclear Experimental Reactor (ITER) [2]. In order to evaluate the efficiency of this fuelling method, it is necessary to determine the pellet ablation rate in a plasma.

The ablation of tokamak pellets has been studied using several semi-analytical [3–7] and numerical [8,9] approaches. An inherent limitation of all previous ablation models has been the absence of a self-consistent and rigorous inclusion of the interaction of the ionized ablation flow with the magnetic field. Near the pellet, the ablation is highly resistive, and thus the pressure gradient force largely balances the inertial force resulting in a nearly isotropic flow pattern. Farther downstream, the $\mathbf{J} \times \mathbf{B}$ Lorentz force eventually overwhelms the inertial force, and tends to funnel the flow along the

magnetic field lines, forming a long extended ablation channel. Whether the ablation channel would offer the pellet additional shielding from the incident parallel electron heat flux has remained an open question for a long time.

The main motivation for the present study is to incorporate these MHD effects, the $\mathbf{J} \times \mathbf{B}$ force and the attendant Joule heating. Our strategy will be to exploit the typically low magnetic Reynolds number $R_m = \mu_0 L v \sigma \ll 1$ [5], where L is the length scale, v is the transverse velocity with respect to the magnetic field and σ is the transverse conductivity in the ablation flow near the pellet. This means that near the pellet the magnetic field is only slightly perturbed, $\delta B/B \sim R_m < 1$, as a result of the induced current density generated by the electromotive force associated with the cross-field component of the flow velocity v . And, in the long ablation channel where the flow is frozen to the magnetic field lines, the ablation pressure P has decayed to the point where the magnetic beta $\beta = \mu_0 P / (B^2/2) \ll 1$. Because of these assumptions, which we will verify *a posteriori*, the magnetic field is taken to be

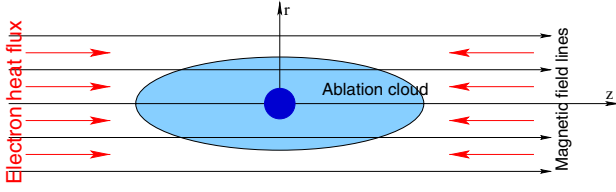


Figure 1. Schematic of the hydrogen pellet in a tokamak.

uniform and constant: its evolution via Faraday’s law is not really needed, either *near the pellet*, where $R_m < 1$, or in the *frozen flow region downstream*, where $\beta < 1$. As a result, the electrostatic MHD approximation is valid.

The knowledge of the pellet ablation rates in magnetic fields and the structure and parameters of the elongated ablation region are also crucial for other models that consider the large-scale drift and redistribution of the ionized ablation substance in a tokamak due to its inherent toroidicity [10–12].

An additional goal of the present paper is to improve modelling and numerical algorithms of [8, 9] by the explicit numerical resolution of interfaces in the pellet–ablation cloud–plasma system. This is done through the FronTier-MHD code for multiphase systems with free interface support [13] based on the method of front tracking [14]. Since the method of front tracking allows the study of multiphysics phenomena in multiphase systems characterized by strong discontinuities in physical properties of the system components, it is ideally suitable to the pellet ablation problem. Another advantage of our code compared with the previous pellet ablation numerical models is that the FronTier-MHD has been implemented in 3D. The 2D axisymmetric approximation is sufficient for the purpose of the present paper. A general 3D study of the pellet ablation and striation instabilities based on an electrostatic model [15] will be reported in a forthcoming paper.

In our computational model, explicit interfaces separate the solid pellet from the ablated gas and the cold, dense and weakly ionized ablation cloud from the highly conducting fusion plasma (see figure 1). This allows the use of different mathematical and numerical approximations in complex geometrical domains occupied by different material substances, and thus the resolution of different material properties and time scales. We assume the axial symmetry of the problem, and solve equations in the cylindrical axisymmetric coordinate system r, z . Realistic equations of state are employed in different geometrical regions corresponding to different states of matter. The code is capable of simulating the transition of deuterium in the pellet from the solid to the liquid state under high ablation pressures. A surface ablation model is used at the pellet surface to model the solid–vapour transition phase change. A kinetic-based electron heat flux model for the calculation of the thermal energy deposition in the ablation cloud and on the pellet surface uses the analytical model of [9, 10]. Atomic physics processes in the ablation cloud such as dissociation, recombination and ionization are taken into account by a plasma equation of state (EOS). In this work, we neglected the rotation of the ablation channel about the axis of symmetry. Modelling of the channel rotation and the study of its influence on the channel width and the pellet ablation rate will be the subject of future work. We have validated the developed model by comparison with

analytical predictions and previous numerical simulations of pure hydrodynamic models (no MHD forces), and used it to study the pellet ablation physics, i.e. the structure of the ablation flow and pellet ablation rates in magnetic fields.

The paper is organized as follows. In section 2, we describe equations for one-fluid MHD in low magnetic Reynolds number approximation, weakly ionized plasma EOS, electronic heat flux and surface ablation models. The numerical implementation and main ideas of the front tracking code FronTier are described in section 3. In section 4, we validate our pellet ablation numerical model through comparisons of 1D and 2D simulations with theory and numerical simulations. After validation, we present MHD studies and discuss ablation channel properties and pellet ablation rates. Finally, we conclude the paper with a summary of our results and perspectives for future work.

2. Main equations

2.1. One-fluid MHD in the low magnetic Reynolds number approximation

Following our discussion in the previous section, we approximate MHD processes in the pellet ablation cloud by the low magnetic Reynolds number MHD. Such an approximation is also beneficial from a numerical point of view, as the fast diffusion of the magnetic field into the cold neutral or weakly ionized ablation cloud would otherwise severely restrict the time step in numerical simulations. The main equations of the inviscid low magnetic Reynolds number one-fluid MHD are the Euler equations with electromagnetic terms:

$$\frac{\partial \rho}{\partial t} = -\nabla \cdot (\rho \mathbf{u}), \quad (1)$$

$$\rho \left(\frac{\partial}{\partial t} + \mathbf{u} \cdot \nabla \right) \mathbf{u} = -\nabla P + \mathbf{J} \times \mathbf{B}, \quad (2)$$

$$\rho \left(\frac{\partial}{\partial t} + \mathbf{u} \cdot \nabla \right) e = -P \nabla \cdot \mathbf{u} + \frac{1}{\sigma} \mathbf{J}^2 - \nabla \cdot \mathbf{q}, \quad (3)$$

$$P = P(\rho, e). \quad (4)$$

Here \mathbf{u} , ρ and e are the velocity, density and the specific internal energy of the fluid, respectively, P is the pressure, \mathbf{B} is the magnetic field induction, \mathbf{J} is the current density distribution and σ is the fluid conductivity. An external heat source $-\nabla \cdot \mathbf{q}$ represents electron heat flux in the pellet ablation problem. We have neglected the heat conduction in the energy equation. The EOS (4) closes the hydrodynamics system. The EOS model for weakly ionized plasmas will be discussed in section 2.2. The current density distribution is obtained using Ohm’s law

$$\mathbf{J} = \sigma(-\nabla \phi + \mathbf{u} \times \mathbf{B}). \quad (5)$$

In this paper, we do not resolve the distribution of the electric field potential in the ablation channel. The pellet cloud charging model is our current work in progress. In the axial symmetry approximation, $\partial/\partial\theta = 0$, where θ is the azimuthal coordinate, the magnetic field is a constant field in the z -direction, $B_z \hat{z}$, and we assume that the only non-zero component of \mathbf{J} is J_θ

$$J_\theta = \sigma u_r B_z. \quad (6)$$

Therefore by neglecting Faraday's law the electrostatic MHD model presented here differs from the one based on the complete MHD system. Consequently, the $\mathbf{J} \times \mathbf{B}$ force can modify the flow, but the induced currents cannot significantly perturb the magnetic field, which remains approximately constant and equal to the background field. In section 4.2 we will justify this approach by presenting calculated values of the cloud β and R_m and discuss its applicability range.

The transverse to \mathbf{B} electrical conductivity of partially ionized plasmas can be approximated by the following expression which includes the effect of electron-ion and electron-neutral atom collisions [5]:

$$\sigma \left[\frac{\Omega}{\text{m}} \right] = \frac{9.675 \times 10^3}{\ln \Lambda T_e [\text{eV}]^{-3/2} + 0.054 T_e [\text{eV}]^{-0.059} (1/f_i - 1)}, \quad (7)$$

where f_i is the ionization fraction, T_e is the electron temperature in eV units and

$$\Lambda = \frac{3.6 \times 10^9 T_e^{3/2}}{n_e^{1/2}}, \quad (8)$$

where n_e is the electron density. In the limit $f_i \rightarrow 1$, $\sigma \rightarrow \sigma_\perp$, which is the transverse Spitzer conductivity.

2.2. Equation of state

The processes of dissociation and ionization in diatomic gases in the presence of external energies, resulting in the formation of weakly ionized plasmas, introduce energy sinks and therefore strongly affect the plasma temperature. This in turn influences the electrical conductivity and MHD processes. In the one temperature, one pressure MHD model, the pressure and specific internal energy of a partially dissociated and partially ionized diatomic gas can be written [4, 9] as

$$P = \left(\frac{1}{2} + \frac{1}{2} f_d + f_i \right) \frac{\rho k T}{m}, \quad (9)$$

$$e = \left(\frac{1 - f_d}{2(\gamma_m - 1)} + \frac{f_d + f_i}{\gamma - 1} \right) \frac{kT}{m} + \frac{1}{2} f_d \frac{k\epsilon_d}{m} + f_i \frac{k\epsilon_i}{m}, \quad (10)$$

where γ_m and $\gamma = 5/3$ are specific heat ratios for molecules and atoms, respectively, k is the Boltzmann constant, m is the mass of the atom (ion). The dissociation $f_d(\rho, T)$ and ionization $f_i(\rho, T)$ fractions are defined as

$$f_d = (n_a + n_i)/n_t,$$

$$f_i = n_i/n_t,$$

in which $n_t \equiv 2n_g + n_a + n_i = \rho/m$ stands for the total number density of *nuclei*, and n_g , n_a and n_i denote, respectively, the number densities of gas D_2 molecules, D atoms and D^+ ions. For deuterium, the dissociation energy is $\epsilon_d = 4.48$ eV and the ionization energy is $\epsilon_i = 13.6$ eV. The dissociation and ionization fractions can be found from Saha equations [16]. For deuterium, they can be written (in eV units) as [4, 9]

$$\frac{f_i^2}{1 - f_i} = 3.0 \times 10^{21} \frac{T^{\alpha_i}}{n_t} \exp\left(-\frac{\epsilon_i}{T}\right), \quad (11)$$

$$\frac{f_d^2}{1 - f_d} = 1.55 \times 10^{24} \frac{T^{\alpha_d}}{n_t} \exp\left(-\frac{\epsilon_d}{T}\right), \quad (12)$$

where $\alpha_i = 3/2$ and the parameter α_d is chosen to be 0.327, as in [4, 9], for the best approximation of deuterium thermodynamic data [4]. The system of equations (9)–(12) can be used as an EOS closure for a hydrodynamic system of equations written in ρ , \mathbf{u} , T independent variables, as well as for a simple finite difference discretization of such a system. The system (9)–(12) is an example of the incomplete EOS model [18]. However, most advanced numerical discretization algorithms, including second order MUSCL type schemes and interface propagation algorithms implemented in the FronTier code [17], are based on solutions of Riemann problems. Solving numerically a Riemann problem requires an ability to calculate the sound speed and integrals of Riemann invariant type expressions along the characteristics. For this purpose, we derived the expressions for entropy and other thermodynamic properties of the system (9)–(12) based on the second law of thermodynamics. Omitting lengthy calculations, we summarize our results.

The molar entropy is given by

$$\frac{S}{R} = \frac{\ln T}{2(\gamma_m - 1)} + \frac{\ln V}{2} + \frac{1 + \beta_d}{2} f_d + (1 + \beta_i) f_i - \frac{\ln(1 - f_d)}{2} - \ln(1 - f_i), \quad (13)$$

where R is the universal gas constant, and

$$\beta_d = \alpha_d + \frac{\epsilon_d}{T},$$

$$\beta_i = \alpha_i + \frac{\epsilon_i}{T}.$$

Using this expression, we can calculate the adiabatic sound speed. For convenience, we introduce an effective gamma, γ_{eff} , that defines the sound speed squared

$$c^2 = \left. \frac{\partial P}{\partial \rho} \right|_S$$

in a form typical for the polytropic gas

$$c^2 = \gamma_{\text{eff}} \frac{P}{\rho}. \quad (14)$$

The explicit expression for γ_{eff} is

$$\gamma_{\text{eff}} - 1 = \frac{(m + a)(1 + (\phi_d \beta_d + \phi_i \beta_i)/(m + a))^2}{(1/(\gamma - 1))m + \frac{3}{2}a + \phi_d \beta_d^2 + \phi_i \beta_i^2} - \frac{\phi_d + \phi_i}{m + a}, \quad (15)$$

where we introduced the following notations

$$\phi_d = \frac{1}{2} \frac{f_d(1 - f_d)}{(2 - f_d)},$$

$$\phi_i = \frac{f_i(1 - f_i)}{(2 - f_i)},$$

$$m = \frac{1 - f_d}{2},$$

$$a = f_d + f_i.$$

The Grüneisen coefficient [18],

$$\Gamma = -\frac{V}{T} \left. \frac{\partial T}{\partial V} \right|_S,$$

used in FronTier EOS and hyperbolic solvers libraries for the calculation of eigenvalues and eigenvectors of Euler's equations, can be expressed as

$$\Gamma = \frac{m + a + \phi_d \beta_d + \phi_i \beta_i}{(1/(\gamma - 1))m + \frac{3}{2}a + \phi_d \beta_d^2 + \phi_i \beta_i^2}.$$

We have also found (see [appendix A](#)) that the fundamental law of thermodynamics imposes the following constraints on the exponents in the Saha equations (11)–(12):

$$\alpha_d = 3 - \frac{1}{\gamma_m - 1}, \quad \alpha_i = \frac{3}{2}.$$

Therefore, in order to satisfy the first constraint with empirical $\alpha_d = 0.327$, we use $\gamma_m = 1.3741$ in our calculations. Not surprisingly, this value of the specific heat ratio lies midway between 7/5 and 9/7, values that correspond, respectively, to excitations of purely rotational modes and rotational–vibrational modes of a diatomic molecule.

The influence of the dissociation and ionization processes on the gas temperature and conductivity with the increase in the specific internal energy is shown in [figure 2](#). In the vicinity of the dissociation and ionization energies, the temperature exhibits a nonlinear behaviour, leading to much smaller values of both temperature and conductivity. By the ‘conductivity of the polytropic gas’ in [figure 2\(b\)](#), we mean the conductivity calculated using equations (7) and (11), with the temperature given by the polytropic EOS model. The use of temperature calculated by the weakly ionized plasma EOS model in (7) and (11) reduces the conductivity, as shown in [figure 2\(b\)](#). Therefore, the EOS model for the ablation can strongly affect both hydrodynamic and MHD processes in the ablation cloud.

2.3. Electron heat flux model

The electronic heat flux model is identical to the one described in [9, 10]. To be self-contained, we formulate the main model equations below. The heat source $-\nabla \cdot \bar{q}$ coming from the energy deposition by hot long-mean-free-path plasma electrons streaming into the ablation cloud along the magnetic field lines can be approximated analytically as

$$-\nabla \cdot \bar{q} = \frac{q_\infty n_t(r, z) \ln \Lambda}{\tau_\infty} [g(u_+) + g(u_-)], \quad (16)$$

where $g(u) = u^{1/2} K_1(u^{1/2})/4$, and K_1 is the Bessel function of the second kind and

$$q_\infty = \sqrt{\frac{2}{\pi m_e}} n_{e\infty} (kT_{e\infty})^{3/2}.$$

$u_\pm = \tau_\pm / \tau_\infty$ is the dimensionless opacity, where

$$\tau_+(r, z) = \int_{-\infty}^z n_t(r, z') \ln \Lambda dz',$$

$$\tau_-(r, z) = \int_z^\infty n_t(r, z') \ln \Lambda dz'$$

are the respective line integrated densities penetrated by right-going (left-going) electrons arriving at the point (r, z) from infinity, and

$$\tau_\infty = \frac{T_{e\infty}^2}{8\pi e^4}.$$

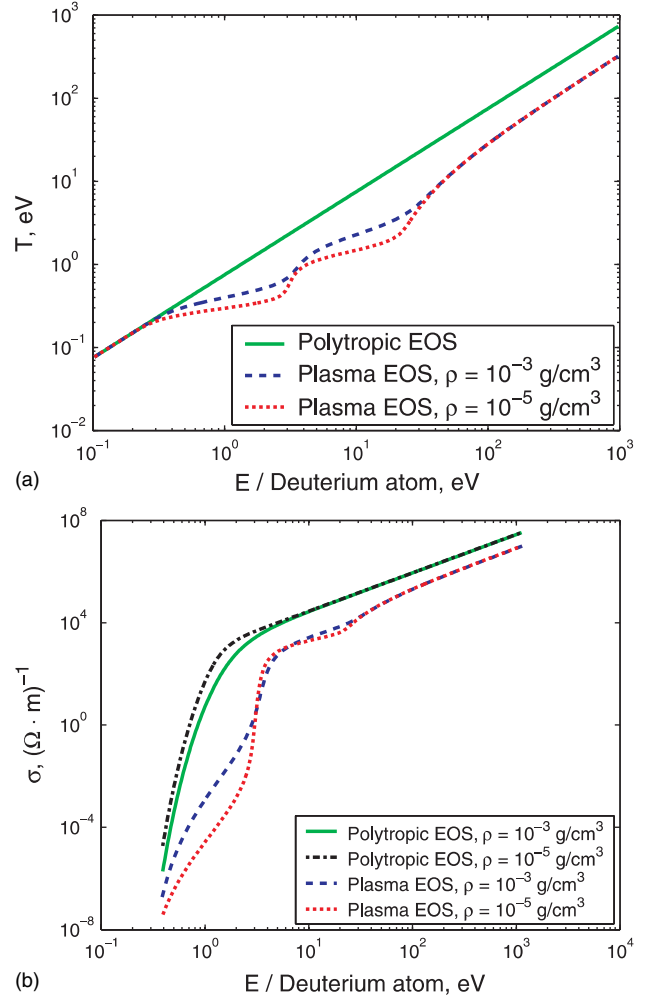


Figure 2. (a) Gas temperature, calculated using the polytropic and weakly ionized plasma EOS models, as a function of the specific internal energy. (b) Plasma conductivity calculated using the temperature of the polytropic and weakly ionized plasma EOS models.

The Coulomb logarithm is

$$\ln \Lambda = f_i \ln \Lambda_{ef} + (1 - f_i) \ln \Lambda_{eb}.$$

For deuterium, Λ_{ef} and Λ_{eb} can be expressed (in eV–cgs units) as

$$\Lambda_{ef} = \frac{1.35 \times 10^{10} T_{e\infty}}{(f_i n_t)^{1/2}}, \quad \Lambda_{eb} = \frac{2.516 T_{e\infty}}{7.5}.$$

The heat deposition on the pellet surface is given as

$$q_\pm = q_\infty \frac{1}{2} u_\pm K_2(u_\pm^{1/2}). \quad (17)$$

2.4. Pellet surface ablation model

It is well known [3–9] that the ablated material effectively shields the pellet surface from the incoming plasma electrons. The dynamics of the pellet ablation is mostly defined by the processes in the ablation cloud, so that surface ablation has a marginal role. We therefore use a simplified model for the cryogenic phase transition on the pellet surface, which

neglects temperature gradients near the interface and some thermodynamic details of the phase transition problem.

Here we assume that all electron energy that reaches the pellet surface is completely used for the conversion of solid deuterium into vapour, thus defining the mass flux. The ablation on the pellet surface satisfies three boundary conditions. First, the heat diffusion in the solid pellet is slow compared with the ablation process, therefore the pellet surface temperature is virtually constant. We varied the pellet temperature between 40 and 60 K and found the ablation process insensitive to the surface temperature, which was in agreement with [9]. Second, with pellet density ρ_{pel} fixed, the normal velocity of the pellet surface, v_s , is determined by the heat flux into the pellet, q , and the sublimation energy ϵ_s . The equation relating q and ϵ_s to the normal velocity of the vapour at the pellet surface u is

$$\frac{q}{\epsilon_s} = -\rho_{\text{pel}}v_s = \rho_v(u - v_s),$$

where ρ_v is the vapour density at the pellet surface and the surface velocity v_s is negative because the pellet is shrinking. For 2D simulations with anisotropic (along magnetic field lines) heating, $q = q_{\pm} \cos \theta$, where θ is the angle between the electron flux and the norm of the pellet surface. The third equation is for the change in the Riemann variable along the characteristic from the ablation cloud onto the pellet surface,

$$\frac{\partial p}{\partial t} + (u - c) \frac{\partial p}{\partial n} - \rho c \left(\frac{\partial u}{\partial t} + (u - c) \frac{\partial u}{\partial n} \right) = \Gamma \frac{\partial q_{\pm}}{\partial z},$$

where c is the sound speed in the cloud, Γ is the Grüneisen coefficient, defined in section 2.2, and z is the direction of the electron flux. Combined with these three boundary conditions, the conservation laws in the cloud completely determine the ablation process.

3. Numerical Implementation

In this section, we will describe numerical ideas implemented in the FrontTier-MHD code. In general, the system of MHD equations in the low magnetic Reynolds number approximation is a coupled hyperbolic–elliptic system in a geometrically complex moving domain. The numerical method treats the MHD system in an operator splitting manner. Namely, we decouple the hyperbolic and elliptic parts of the MHD system for every time step. The mass, momentum and energy conservation equations are solved first without the electromagnetic terms (Lorentz force). We use the front tracking hydro code FrontTier with free interface support [17,19] for solving the hyperbolic subsystem. The electromagnetic terms are then found, in the general case, from the solution of the Poisson equation for the electric potential. In our 2D axisymmetric approximation, the numerical solution of the Poisson problem is eliminated as the current density in the ablation cloud is a known function of the radial velocity and longitudinal magnetic field, as was explained in section 2.1. At the end of the time step, the fluid states are integrated along every grid line in the longitudinal direction in order to obtain the electron heat deposition given by equations of section 2.3. The heat deposition changes the internal energy and temperature of fluid states and therefore

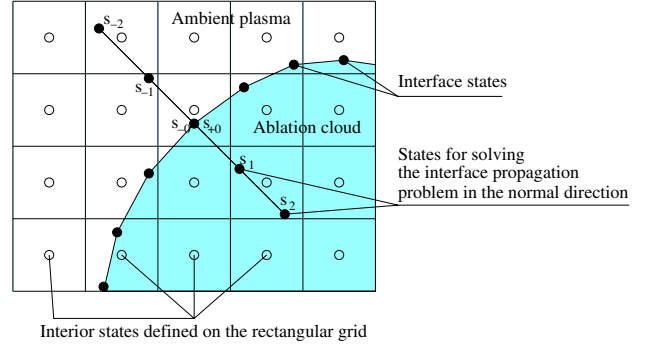


Figure 3. Rectangular grid, interface and states for the method of front tracking. States contain density, momentum and energy density of the fluid (plasma), and references to the EOS model and other parameters.

the electrical conductivity. The Lorentz force is then added to the momentum equation.

FrontTier represents interfaces as lower dimensional meshes moving through a volume filling grid [14], as shown in figure 3. The traditional volume filling finite difference grid supports smooth solutions located in the region between interfaces. The location of the discontinuity and the jump in the solution variables are defined on the lower dimensional grid or interface. The dynamics of the interface comes from the mathematical theory of the Riemann problem. The Riemann problem consists of finding solutions to the system of conservation laws, which in our case is the system of Euler’s equations, with piece-wise constant initial conditions [18]. The solution of the Riemann problem consists of three elementary waves: the left and right going shock or rarefaction wave, and the middle wave, which is always the contact discontinuity with both pressure and velocity continuous across the wave. Since the multiphase fluid system can be considered as a discontinuous solution of Euler’s equations with discontinuous parameters, the interface separating different phases resembles the contact discontinuity wave of the Riemann problem solution.

The main algorithms implemented in FrontTier’s hyperbolic part are as follows [17]. The time step loop starts with the advance of the interface. A computational stencil is constructed at every interface point in the normal and tangential directions, and stencil states are obtained through interpolation. Then Euler equations, projected on the normal and tangential directions, are solved. The normal propagation of an interface point is a predictor–corrector technique. We solve the Riemann problem for left and right interface states to predict the location and states of the interface at the next time step. Then a corrector technique is employed which accounts for fluid gradients on both sides of the interface. Namely, we trace back characteristics from the predicted new interface location and then solve Euler equations along the characteristics using techniques described in [17]. After the propagation of the interface points, the new interface is checked for consistency of intersections. The untangling of the interface at this stage consists in removing unphysical intersections, and rebuilding a topologically correct interface [19]. The update of interior states using second order monotonic upstream-centred schemes for conservation laws (MUSCL, [20,21]) is performed

in the next step. The tracked interface allows us to avoid the integration across large discontinuities of fluid states and thus eliminate the numerical diffusion. Additional features of the FronTier hyperbolic solvers include a choice of exact or approximate Riemann solvers and realistic models for the EOS.

We would also like to comment on some implementation details of the EOS model for weakly ionized plasmas described in section 2.2. To satisfy the requirement of FronTier's hyperbolic solvers and interface propagation routines, we derived the complete set of thermodynamic functions in terms of different pairs of independent variables (ρ, e) , (ρ, P) , (ρ, T) , etc. The corresponding algorithms use numerical solvers for complicated nonlinear algebraic equations. The direct use of such algorithms in hydrodynamic simulations was prohibitively expensive. To speed up the code, we created tabulated data of thermodynamic functions and their integrals on a fine mesh in the specific domain of interest before simulations and used table look-up and interpolation algorithms during the run.

4. Simulation results

In this section, we apply the front tracking numerical model to the study of the pellet ablation and hydrodynamic/MHD processes in the ablation cloud in 1D spherically symmetric and 2D axisymmetric geometries. In the next sections, the term ‘*hydrodynamic model*’ indicates that the electromagnetic $(\mathbf{J} \times \mathbf{B})$ force is ignored, contrarily to the ‘*MHD model*’. The 1D hydrodynamic model of section 4.1.1 is used primarily for the benchmark purpose. The axisymmetric 2D hydrodynamic model, described in section 4.1.2, employs the anisotropic heating along imaginary magnetic field lines. This model was studied in detail in [8, 9]. Using this model primarily for the benchmark, we also obtained new results on the role of the anisotropic heating in the ablation rate reduction. The study of the axisymmetric MHD model, summarized in section 4.2, is the main goal of this paper. We discuss the formation and properties of ablation channels in magnetic fields of various strength, flow structures in channels and the reduction of the pellet ablation rate by magnetic fields.

Unless otherwise stated, we use the following parameters for our simulations: the pellet radius $r_p = 2$ mm, plasma electron temperature $T_{e\infty} = 2$ keV, plasma number density $n_{e\infty} = 10^{14}$ cm $^{-3}$ and the pellet density $\rho_{pel} = 0.2$ g cm $^{-3}$.

In previous pellet injection experiments with realistic plasma profiles and pellet speeds ~ 800 m s $^{-1}$, the heat flux seen by the moving pellet is actually ramping up on a time scale on the order of the pellet lifetime ~ 300 – 600 μ s. In fusion devices such as ITER, a pellet travels through a high temperature gradient plasma pedestal region during a time anywhere from 20 to 300 μ s. We define a ‘warm-up’ time, during which we linearly ramp up the incident electron heat flux q_∞ from 0 to its maximal value in order to simulate the heat flux seen by the moving pellet. For the purely hydrodynamic simulations (no $\mathbf{J} \times \mathbf{B}$ force) the warm-up time has no effect on the formation of the steady-state ablation flow. To reduce the computation time, we choose a 1 μ s warm-up time.

When the $\mathbf{J} \times \mathbf{B}$ force is included, the formation of the ablation channel is quite sensitive to the warm-up time. We shall see explicitly why the ablation rate of the pellet at a

given moment in time depends not only on the heat flux at that moment but also on its past exposure to the time-varying heat flux at all earlier moments. Loosely speaking, the pellet ablation process has ‘memory’, and therefore it matters how long it takes for the heat flux to ramp up to the maximum value. However, simulations of very long physical time intervals currently require a very long computational time even on large parallel supercomputers due to the restriction of the time step imposed by the stability condition. To speed up the computational time, we restricted the MHD simulations to artificially short warm-up times, typically in the range from 5 to 20 μ s.

The 2D axisymmetric MHD model required one additional parameter, namely the effective shielding length of the cloud [22, 23]. The actual shape of the ablation channel in a real tokamak magnetic field ($\nabla \mathbf{B}$ induced bending of the channel) can be studied only in 3D. The assumption of a perfectly axisymmetric channel would lead to an increase in the shielding of the pellet, causing the ablation rate to approach zero asymptotically in time. To eliminate these unphysical consequences, we used estimates of [22, 23] to obtain the effective shielding length of 15 cm. Numerically, we limited the interaction of the ablation channel with the plasma heat flux to 15 cm, and applied the outflow boundary conditions in the z -direction. In other words, to simulate a finite shielding length, or heating zone, heat flux absorption in the region $z > 15$ cm was arbitrarily set to zero. The effective shielding length was also assumed to be constant as we varied the magnetic field over the range 2–6 T.

4.1. Pellet ablation studies with hydrodynamic models

4.1.1. Spherically symmetric model. 1D axially symmetric simulations of the pellet ablation confirmed the analytical [3] and previous numerical [8, 9] predictions of the steady-state ablation flow. In the first numerical experiment, the atomic processes in the ablation cloud were ignored by using the polytropic EOS for molecular gas with $\gamma = 7/5$. The ablation flow reached the steady-state ablation rate of $G = 112$ g s $^{-1}$ in a few (< 5) microseconds. The ablation rate was in very good agreement with the result of Ishizaki *et al* : $G = 113$ g s $^{-1}$ was reported in [9]. The ablation flow transformed from a subsonic regime near the pellet surface to a supersonic one at the sonic radius $r^* = 0.659$ cm. The pressure and temperature at the sonic radius were $p^* = 20.0$ bar and $T^* = 5.51$ eV, respectively. Figure 4(a) shows the normalized pressure p/p^* , temperature T/T^* and Mach number M as functions of the normalized radius r/r^* . We found that the Mach number asymptotically approaches

$$M_\infty = \sqrt{\frac{5}{\gamma}} = 1.8898, \quad (18)$$

as predicted in [3] and also verified in previous numerical studies [8, 9]. We have compared simulation data with some scaling laws derived in [3], such as the proportionality of the ablation rate to $r_p^{4/3}$, and found good agreement.

The next simulation accounted for atomic processes in the ablation cloud through the use of the plasma EOS model described in section 2.2. A small reduction of the ablation rate

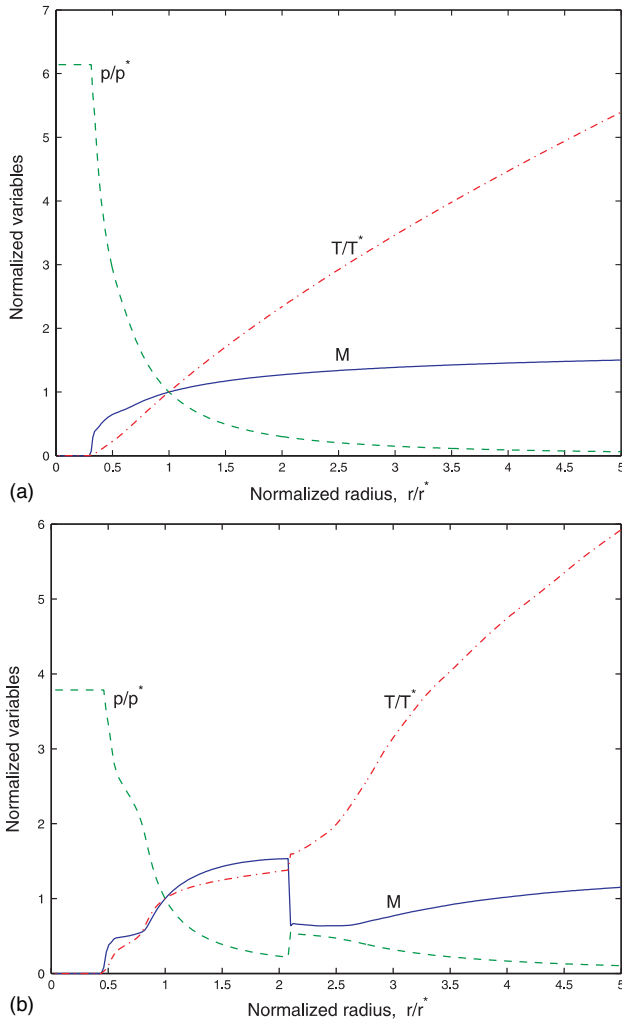


Figure 4. Normalized ablated gas profiles at $10 \mu\text{s}$ in 1D spherically symmetric model of (a) ablation without atomic processes (polytropic EOS) and (b) with atomic processes (plasma EOS). The solid, dashed and dash-dotted lines are M , p/p^* and T/T^* as functions of r/r^* , respectively.

was observed, in complete agreement with [9]. The absolute value of the ablation rate $G = 106.5 \text{ g s}^{-1}$ was practically identical to $G = 106 \text{ g s}^{-1}$ obtained in [9]. The first sonic radius, $r^* = 0.445 \text{ cm}$, was shifted towards the pellet surface compared with the previous simulation for which the atomic processes in the ablation cloud were ignored. The pressure and temperature at the sonic radius were, respectively, $p^* = 26.9 \text{ bar}$ and $T^* = 1.07 \text{ eV}$ ($T^* = 1.11 \text{ eV}$ was reported in [9]). The normalized pressure, temperature and Mach numbers are depicted in figure 4(b). From the figure, it is clear that the ablation phenomena are changed by including the atomic processes. The most essential difference is a shock wave, represented by a jump structure at $r = 2.1r^*$, in figure 4(b). The stationary shock front is due to the energy sink from the atomic processes. The ablated material accelerates near the pellet surface and the temperature increases due to external heating. As the ablated gas becomes sufficiently hot, the dissociation and ionization take place. A portion of the energy of incoming hot electrons is used for the atomic processes rather than for the thermal and kinetic energy increase. This

causes the shock wave. Farther downstream, we observed a second transonic surface at $r = 3.9r^*$. The double transonic flow structure was also observed in [9].

4.1.2. Axisymmetric hydrodynamic model. In this section, we present results of numerical studies of the axisymmetric hydrodynamic model. We remind the reader that the only action of the magnetic field was to direct the electronic heat flux along the z -axis. The MHD model, accounting for the $\mathbf{J} \times \mathbf{B}$ force, will be discussed in the next section. The pellet deformation under high ablation pressures was not studied in the current paper. In order to prevent deformation, we artificially set to zero the velocity of the fluid states inside the pellet and only propagated the pellet surface points according to the surface ablation model (‘rigid’ pellet model). Another reason for not considering the pellet deformation is that real tokamaks operate with cylindrical pellets with their axis of symmetry not aligned with the magnetic field lines. Therefore, 3D simulations are required in order to account for the real pellet shape. Our 3D studies will be reported in a future paper.

2D distributions of the temperature, pressure and Mach number of the ablation flow near the pellet at $20 \mu\text{s}$ are shown in figure 5, and plots of the temperature, pressure and Mach number in the longitudinal and radial directions are shown in figure 6. Figure 5(c) shows that the double transonic flow in the spherical model with atomic processes in the ablation cloud is preserved in the axisymmetric hydrodynamic model. The flow is established within few microseconds, but it takes at least $20 \mu\text{s}$ for the ablation rate to reach the steady-state value (much longer compared with the 1D model). It can be seen in figure 5(c) that the two sonic surfaces and the shock front in between are close to spherical shapes, with the first sonic surface being slightly elongated in the $z = 0$ plane (the first sonic point was located at 0.504 cm in the radial direction and at 0.445 cm along the z -axis), and the shock and the second sonic surfaces being slightly elongated along the z axis. This is consistent with results of [9].

Figure 6 allows us to compare properties of the ablation flow in the longitudinal and radial directions. Figure 6(a) shows that the temperature beyond the shock surface is about 57% higher along the r -axis than along the z -axis. Higher temperatures in the radial direction can be explained by the pellet ‘shadow’: the region $r \leq r_p$ aligned with the axis of symmetry. Hot electrons that reach the pellet are deposited on the pellet surface, providing the energy source for ablation. Therefore, hot electrons going in only one direction deposit energy in the shadowed volume of the ablation cloud, as opposite to the ablation cloud region $r > r_p$. From figure 6(b) we observe that cloud pressure is isotropic except near the pellet surface. The pressure on the pellet surface is 108 bar at the poles and approximately 75 bar on the equator. The reason for the pressure gradient along the pellet surface is that the heat flux penetrating the ablation cloud is entirely absorbed by the pellet at the poles, while only marginally absorbed on the equator. Lastly, figure 6(c) indicates that the Mach number is virtually the same in two directions.

The steady-state value of the ablation rate was 90.5 g s^{-1} . This result is in excellent agreement with the numerical simulation of [8] and the semi-analytic 2D model of Kuteev

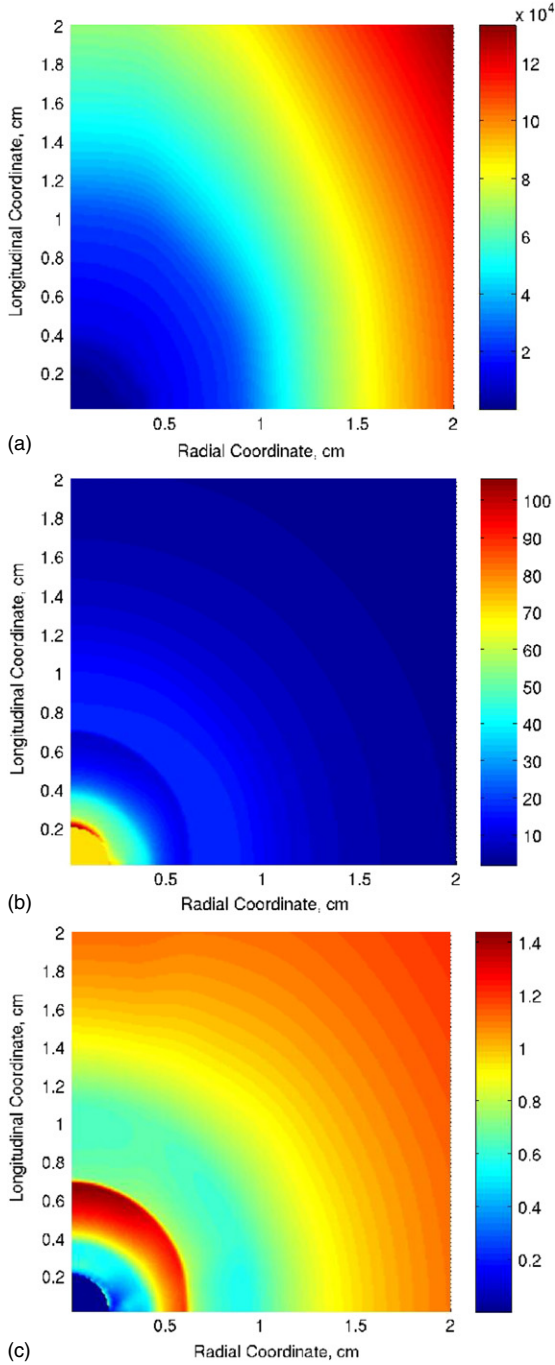


Figure 5. 2D distributions of (a) temperature (eV), (b) pressure (bar) and (c) Mach number of the ablation flow near the pellet at $20 \mu\text{s}$ obtained with the 2D axisymmetric hydrodynamic model.

[6]: both references obtain $\sim 90 \text{ g s}^{-1}$. Our result is not in agreement with the numerical simulation of [9], which obtains a lower result of 60 g s^{-1} . Accordingly, we find a 0.85, or 15%, reduction in ablation rate compared with our 1D spherically symmetric simulation. We conducted a series of 1D spherically symmetric and 2D axially symmetric hydrodynamic simulations at different values of the electron plasma density and temperature in order to quantify the heating anisotropy on pellet ablation. The reduction of the ablation rate by 2D effects was consistently found to be, on average, ~ 0.82 or $\sim 18\%$. This number appears to

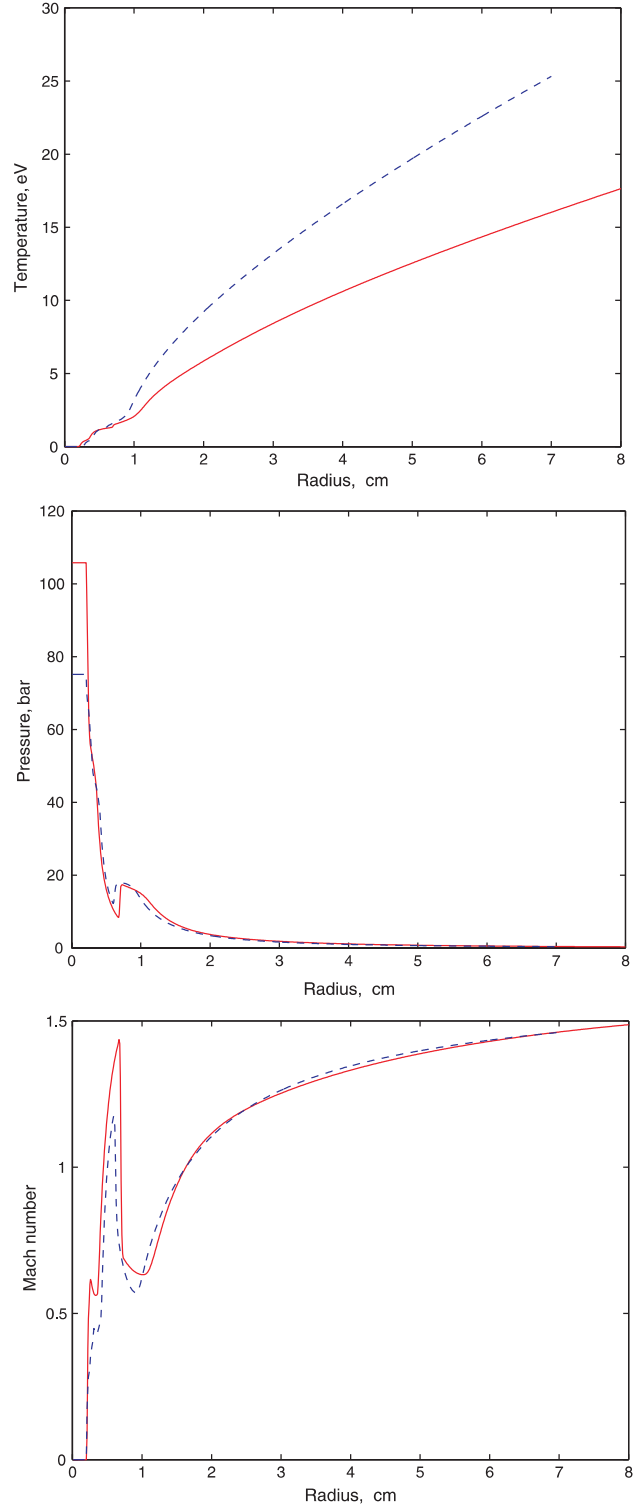


Figure 6. (a) Temperature (eV), (b) pressure (bar) and (c) Mach number of the ablation flow near the pellet in the longitudinal (solid line) and radial (dashed line) directions at $20 \mu\text{s}$ obtained with the 2D axisymmetric hydrodynamic model.

conflict with the prevailing expectation that 2D ablation rates are reduced by a factor of ~ 2 compared with 1D ablation rates [6, 8, 9].

Arguably, the factor of ~ 2 reduction must now be called into question. First of all, our 2D results agree with [6, 8].

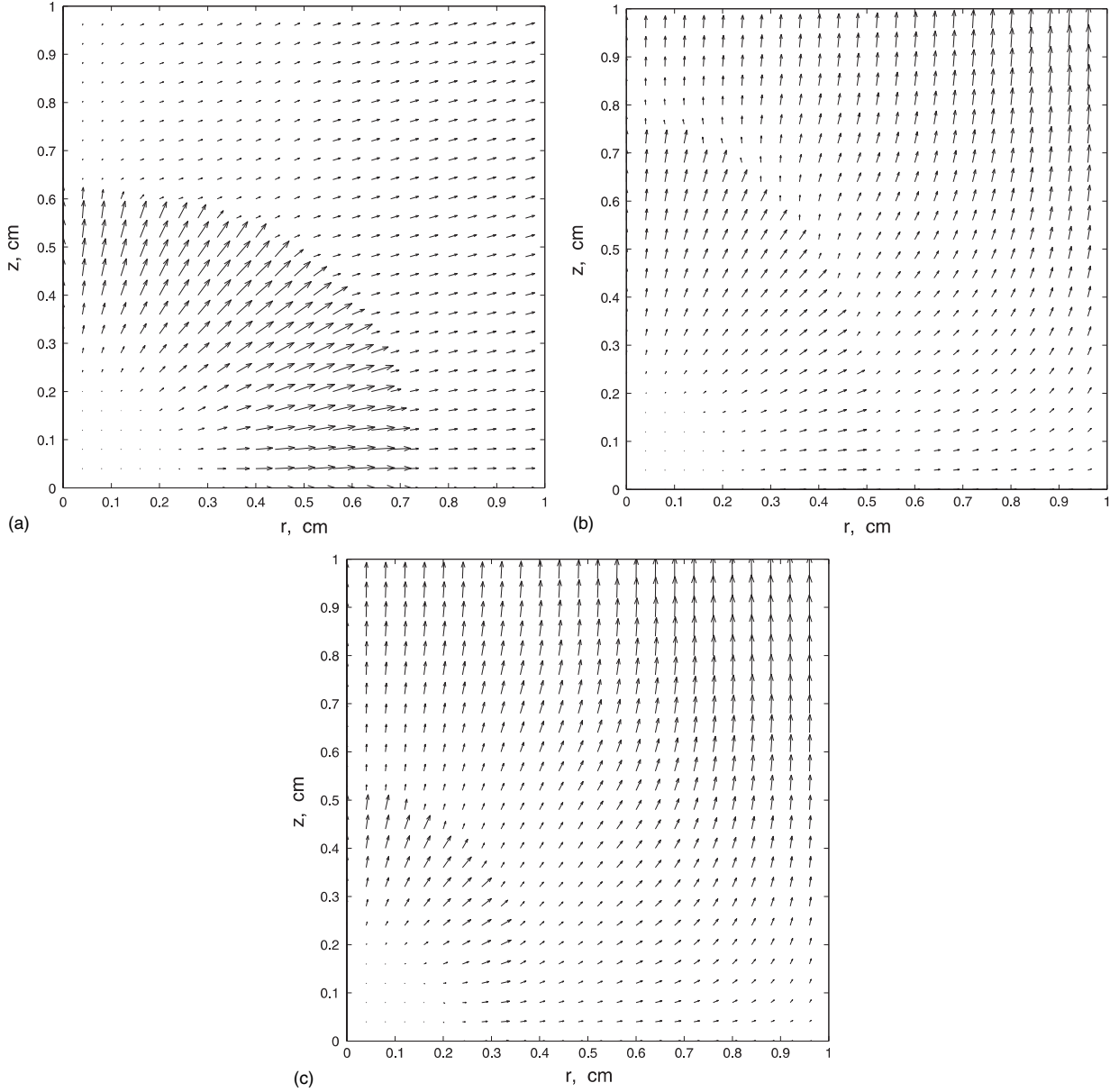


Figure 7. Velocity distribution of the ablation flow near the pellet in 6 T magnetic field with warm-up time $20 \mu\text{s}$. (a) $1 \mu\text{s}$, (b) $3 \mu\text{s}$ and (c) $5 \mu\text{s}$.

Despite the implied claims of factor of 2 reduction, a clear-cut confirmation was unavailable because neither reference presented 1D simulations on hydrogen pellet ablation with a Maxwellian electron heat flux. What [6] actually found was that their 2D pellet ablation rate was a factor of ~ 2 (actually 2.2) higher than the transonic flow model of [3]: [6] obtained 90 g s^{-1} , and [3] obtained 41 g s^{-1} . According to the authors of [6], the factor of 2.2 discrepancy could be attributed to a combination of two approximations made by [3], the mono-energetic heat flux approximation and the 1D spherically symmetric heating approximation, both removed in [6]. The argument was that the actual Maxwellian heat flux increases the ablation rate by a factor of four or five. It was therefore argued that 2D effects must reduce the ablation rate by a factor of ~ 2 , to explain the net result of a factor of ~ 2.2 larger ablation rate compared with [3]. We believe that this interpretation of the discrepancy is now in doubt. Our explanation

for the discrepancy is that 2D effects account for only a 0.82 reduction in the ablation rate, not ~ 2 . While the effect of using a Maxwellian heat flux compared with a mono-energetic heat flux is to increase the ablation rate by a factor of 2.75. This number comes from the recent 1D simulations presented in section 4 of [9], in which we have considerable confidence because they agree well with our 1D simulations (with Maxwellian heat flux). The net result $2.75 \times 0.82 = 2.25$ nicely explains the factor of 2.2 discrepancy. Finally, even though the 2D simulations of [9] show a factor of ~ 2 reduced ablation rate due to heating anisotropy, these 2D simulations are not in agreement with our 2D result or the 2D results of [6, 8] which we do agree with.

4.2. Axisymmetric MHD model

In this section, we study the influence of MHD forces on the pellet ablation flow. The ionization of the pellet ablation cloud

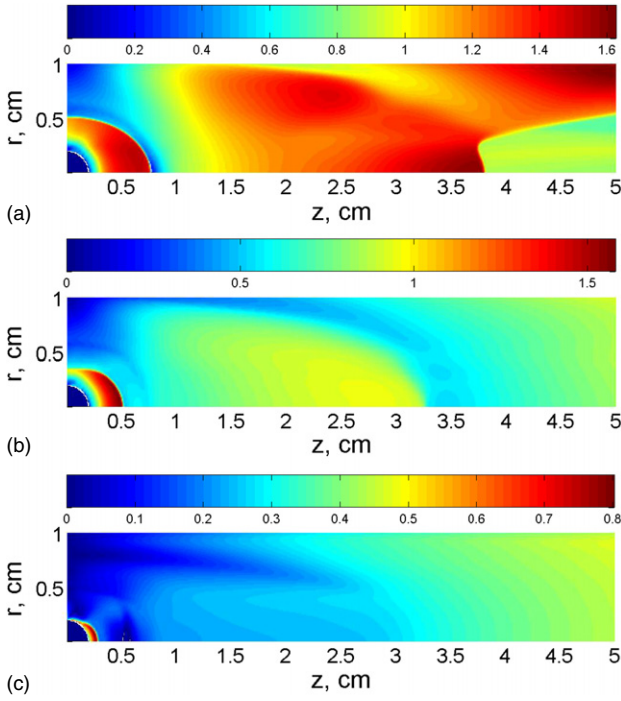


Figure 8. Mach number distribution in the ablation flow near the pellet in 6 T magnetic field with warm-up time $20 \mu\text{s}$. (a) $3 \mu\text{s}$, (b) $5 \mu\text{s}$ and (c) $9 \mu\text{s}$.

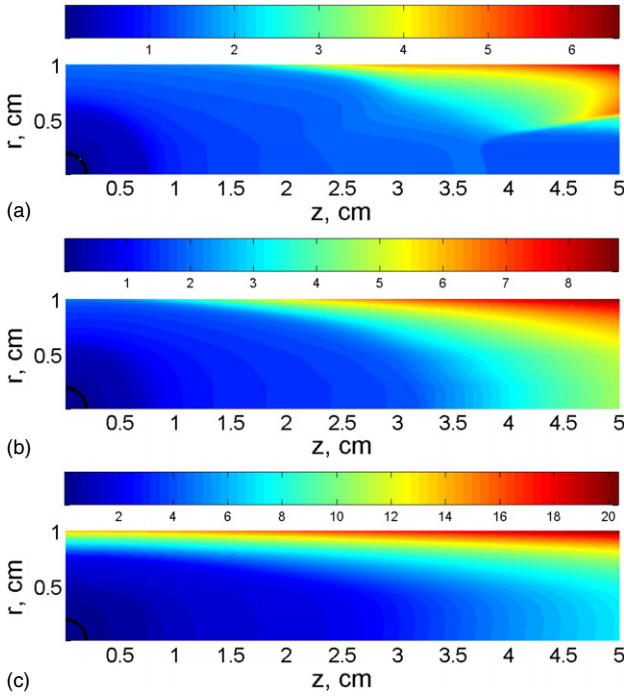


Figure 9. Temperature (eV) distribution in the ablation flow near the pellet in 6 T magnetic field with warm-up time $20 \mu\text{s}$. The dark curve near the origin is the pellet surface. (a) $3 \mu\text{s}$, (b) $5 \mu\text{s}$ and (c) $9 \mu\text{s}$.

by the electron heat flux leads to the channelling of the ablation flow along magnetic field lines. We found that this effect is sensitive to the parameter ‘warm-up time’. Longer warm-up time leads to a slower increase in temperature and wider ablation flow channels.

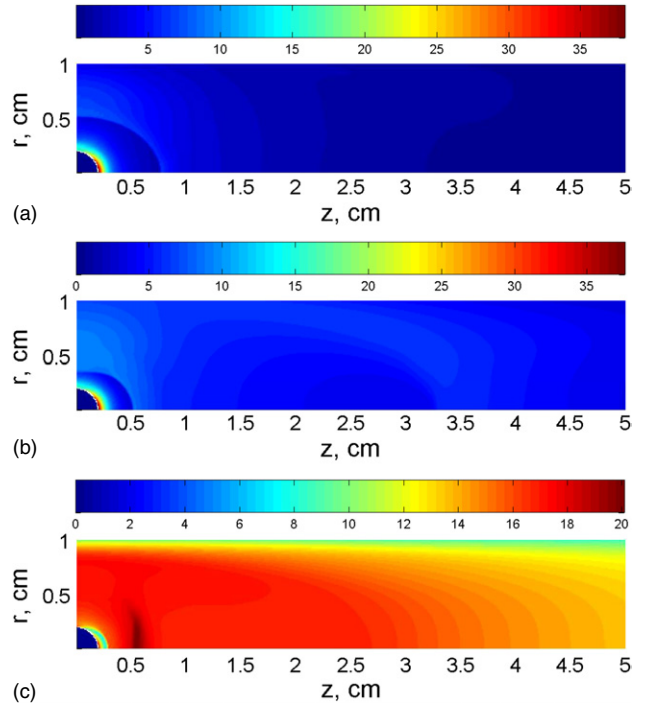


Figure 10. Pressure (bar) distribution in the ablation flow near the pellet in 6 T magnetic field with warm-up time $20 \mu\text{s}$. (a) $3 \mu\text{s}$, (b) $5 \mu\text{s}$ and (c) $9 \mu\text{s}$.

With $20 \mu\text{s}$ warm-up time and 6 T magnetic field, the ablation flow undergoes large changes at approximately $2 \mu\text{s}$ after the ablation process starts at the beginning of warm-up. As shown in figure 7, the ablation flow between the pellet surface and the shock wave was almost spherically symmetric at $1 \mu\text{s}$, with the absolute value of the radial component larger than the longitudinal component (consistent with observations of the previous section), and the flow outside the shock wave was primarily in the radial direction. At $3 \mu\text{s}$, the flow before the shock wave slightly changed its direction towards the z -axis, while the flow outside the shock wave completely changed direction and approximately aligned the magnetic field. Such a flow distribution remained qualitatively unchanged during several microseconds with the sonic and shock surfaces moving towards the pellet surface.

In addition to the formation of the ablation channel, the action of the magnetic field completely changed the structure of the ablation flow compared with the pure hydrodynamic case. Results illustrating this statement are depicted in figures 8–10. The double transonic flow structure, similar to the one predicted by the hydrodynamic model, remained in the ablation channel at $t = 3 \mu\text{s}$ (figure 8(a)). At $t = 5 \mu\text{s}$, the second supersonic layer was transformed into the subsonic regime (figure 8(b)) due to the temperature increase along the ablation channel (figure 9(b)). The first sonic and shock surfaces moved towards the pellet surface. However at $t = 9 \mu\text{s}$, the entire flow in the ablation channel was transformed into subsonic (figure 8(c)). The temperature continued to increase along the ablation channel (figure 9) while the pressure distribution grew to a steady state which is close to constant in the channel except for the narrow region near the pellet surface (figure 10). At shorter warm-up times, the flow exhibits similar

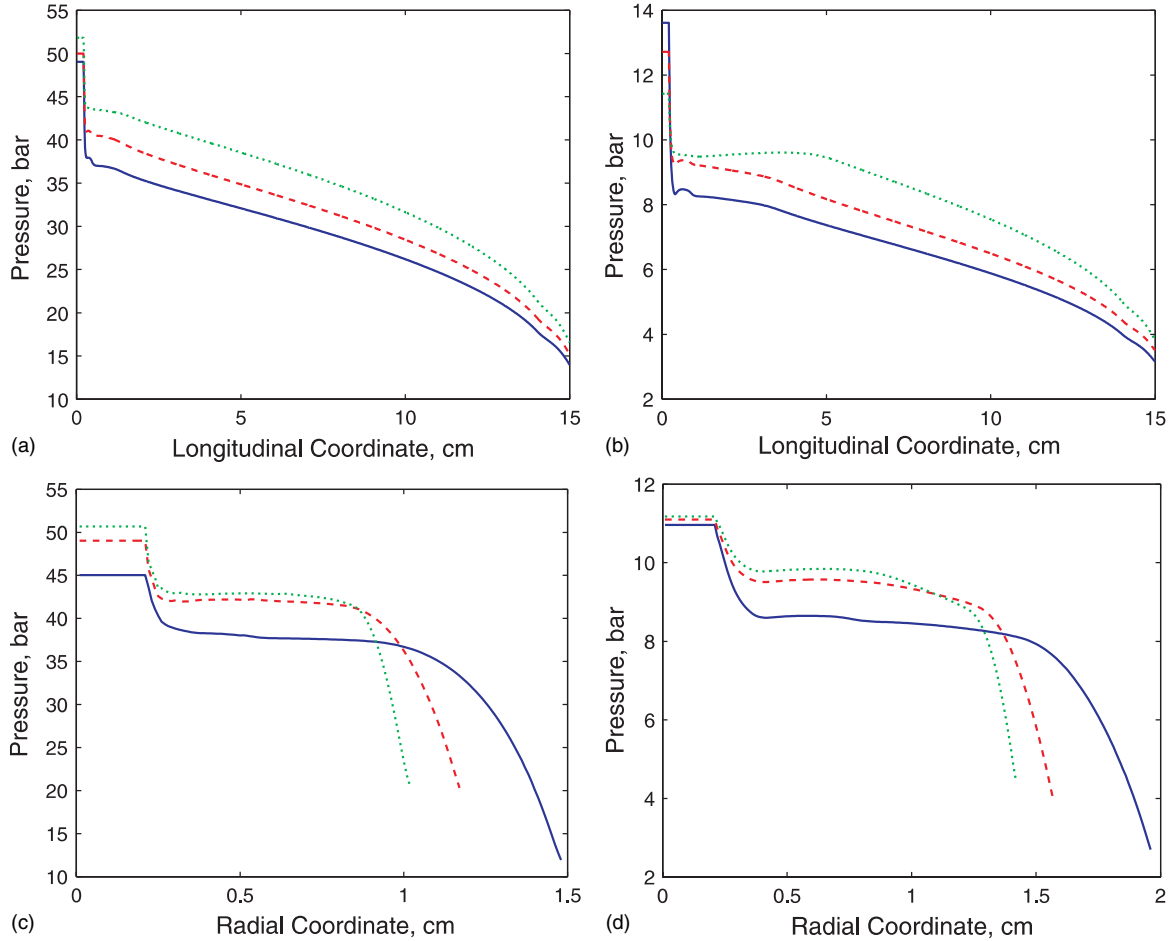


Figure 11. Pressure along the longitudinal and radial axes of steady-state ablation channel with warm-up time $10 \mu\text{s}$. Solid line: $B = 2$ T, dashed line: $B = 4$ T and dotted line: $B = 6$ T. The longitudinal domain extends from the pellet centre to the end of the effective shielding length, and the radial domain extends from the pellet centre to the edge of the ablation channel. (a) Longitudinal, no shielding; (b) longitudinal, electrostatic shielding; (c) radial, no shielding and (d) radial, electrostatic shielding.

qualitative behaviour and transforms into the subsonic regime at an earlier time.

At a given value of the shielding length (15 cm in our simulations) the ablation flow converged into steady state. The pressure, Mach number and temperature along the axis of symmetry and across the ablation channel in the location of the pellet in the steady-state flow are shown in figures 11(a), 11(c)–13(a), 13(c). We define the channel radius to be the location of the highest pressure gradient in the radial direction. These simulations were performed at $10 \mu\text{s}$ warm-up time. The steady-state flow was subsonic everywhere in the channel, with the Mach number reaching 1 at the exit. The pressure was almost constant along the ablation channel, and slowly decreased towards the channel exit. In the transverse direction, the pressure also remained almost constant across the channel and decayed towards the channel edge. The temperature increased in both the longitudinal and the transverse directions, reaching higher values near the edge of the channel than near the channel exit. The nonlinear behaviour of the temperature and Mach number near the pellet surface was caused by the atomic processes in the ablation cloud, similarly as in the 1D hydrodynamic case. In the MHD simulation the flow always remained subsonic inside the channel, so shock waves could not be observed. However, the energy sinks caused by

the dissociation and ionization reduced the kinetic energy and the Mach number of the flow at a distance of order 1 mm from the pellet surface. In the transverse direction on the $z = 0$ mid-plane, we observed the stagnation (zero velocity) point at a small distance behind the ablation channel radius, in agreement with [24].

As pointed out in [9], the negatively charged ablation cloud effectively reduces the incident electron density n_e and the heat flux by the Boltzmann factor $e^{-e\phi/T_{\infty}}$, where ϕ is the potential drop across the cold cloud/hot plasma interface. The pellet charging is not self-consistently modelled in this paper, it will be addressed in future work. We model the effect of the electrostatic shielding by reducing n_e from 10^{14} to $1.6 \times 10^{13} \text{ cm}^{-3}$, according to the theoretical estimate of [9]. The corresponding pressure, Mach number and temperature in the steady-state flow are shown in figures 11(b), 11(d)–13(b), 13(d). As expected, the channel pressure and temperature are significantly lower with electrostatic shielding, while the Mach number profiles are not changed by much. It is worth mentioning that in the case of the electrostatic shielding, the pressure on the pellet surface is significantly reduced and almost isotropic, which leads to a much weaker stress on the solid pellet compared with the pure hydrodynamic case.

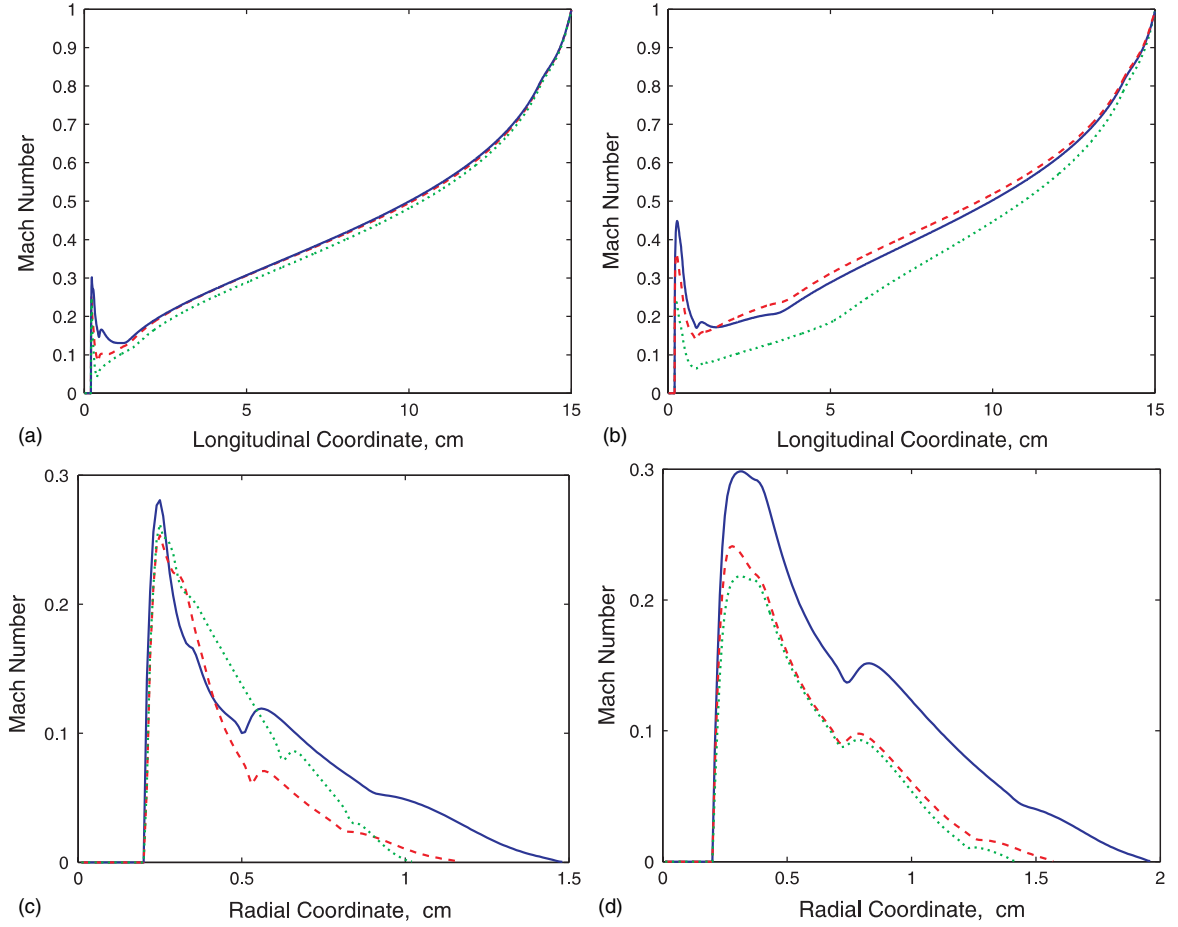


Figure 12. Mach number along the longitudinal and radial axes of the steady-state ablation channel with warm-up time $10 \mu\text{s}$. Solid line: $B = 2$ T, dashed line: $B = 4$ T and dotted line: $B = 6$ T. (a) Longitudinal, no shielding; (b) longitudinal, electrostatic shielding; (c) radial, no shielding and (d) radial, electrostatic shielding.

Note that the pressure slightly decreases towards the exit of the ablation channel. This effect was caused by the model approximations. Namely, we specify the length of the ablation channel to be 15 cm, smoothly decrease to zero the unattenuated electron heat flux Q_∞ in a narrow (1 cm) layer near the channel exit and allow the ablated material to escape the channel. The ablated material rapidly expands reaching the sonic state at the channel exit. This expansion and the reduction of Q_∞ causes the decrease in temperature. Values of the pressure, temperature and Mach number are in agreement with analytical expressions of [10]. The temperature and pressure distributions in the ablation channel normalized by the values at the exit are plotted in figure 14. For comparison, the normalized temperature and pressure predicted by the parallel flow model for the ablation channel [10] are also plotted in figure 14. The agreement between the simulation and the model is excellent except at low Mach number, where the flow is in transition from spherical to parallel.

Measurements of the ablation channel width and ablation rate are shown in figures 15(a) and (b). As expected, the channel width reduced with the increase in the magnetic field and decrease of the warm-up time. Indeed, the magnetic field can only restrict the outward radial motion of the ablated material; it cannot reverse the radial flow

or reduce the ablation channel radius once it is formed (at least for leading order effects as opposite to small pressure perturbations). For smaller warm-up times, the increase in temperature and ionization fraction is slower, and the ablated material expands radially to wider ablation channels before being restricted to the longitudinal motion by the magnetic field. For the same reason, the channel width is larger with reduced electron density flux, though the ablation rate is smaller. For $n_e = 10^{14} \text{ cm}^{-3}$, the ablation rate was approximately 34 g s^{-1} in the 2 T magnetic field, 28 g s^{-1} in the 4 T field and 24 g s^{-1} in the 6 T field. Compared with the ablation rate in the 2D hydrodynamic model, 90 g s^{-1} , that corresponded to the 2.6, 3.2 and 3.8 times reduction. With the electrostatic shielding taken into account, the corresponding ablation rate in the hydrodynamic model was reduced to about 60%. The magnetic field further reduced the ablation rate by 2.5 times to approximately 22 g s^{-1} in the 2 T field, by 2.8 times to 19 g s^{-1} in the 4 T field and by 3.2 times to 17 g s^{-1} in the 6 T field.

Therefore, we conclude that the magnetic field significantly reduces the ablation rate due to the increased shielding of the pellet by long ablation channels contrarily to some expectations that the magnetic field would have a minor effect on the ablation rate as it is mostly the high-density,

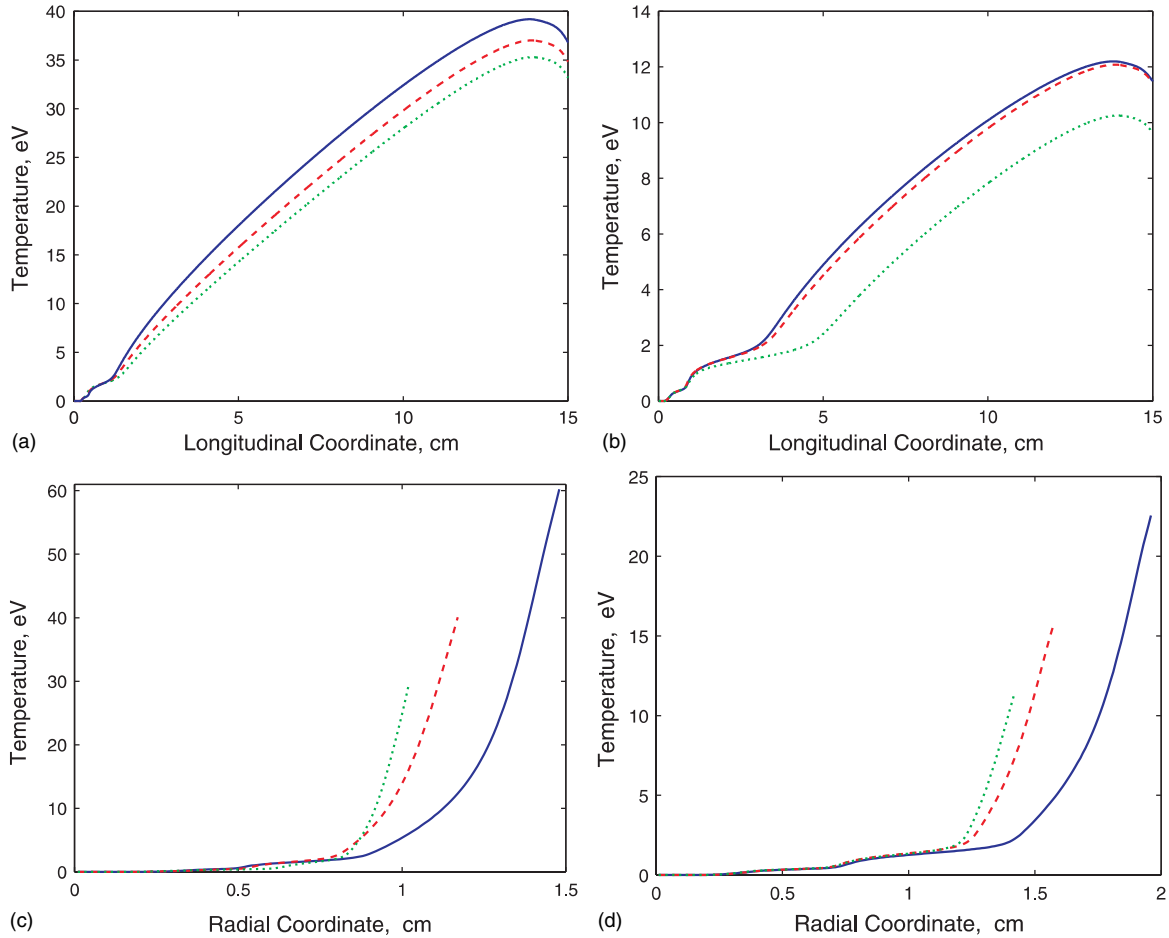


Figure 13. Temperature along the longitudinal and radial axes of steady-state ablation channel with warm-up time $10 \mu\text{s}$. Solid line: $B = 2$ T, dashed line: $B = 4$ T and dotted line: $B = 6$ T. (a) Longitudinal, no shielding; (b) longitudinal, electrostatic shielding; (c) radial, no shielding and (d) radial, electrostatic shielding.

isotropic part of the flow close to the pellet that does most of the shielding. The directional channelling of the ablated material leads to the redistribution of density as shown in figure 16, and a much stronger shielding in the channel far from the pellet compared with the spherically symmetric case.

One important caveat is necessary to interject at this point. We used warm-up times $\sim 10 \mu\text{s}$ that were unrealistically shorter than what is actually expected in present day pellet injection experiments. With realistic plasma profiles and pellet speeds $\sim 800 \text{ m s}^{-1}$, the heat flux seen by the moving pellet actually represents a warm-up time of $0.5 \text{ m} / (800 \text{ m s}^{-1}) \sim 600 \mu\text{s}$. The present simulations showed (see figure 15(b)) that changing the warm-up time from 5 to $10 \mu\text{s}$ increased the ablation rate from 16.5 to 22 g s^{-1} in the 2 T field, from 12.7 to 19 g s^{-1} in the 4 T field and from 10.6 to 17 g s^{-1} in the 6 T field. It indicates that a short warm-up time results in ablation rates that are much lower than experimental values. For example, a warm-up time of $10 \mu\text{s}$ gives an ablation rate of 22 g s^{-1} at 2 T, whereas the experimentally adjusted ablation rate formula of [7] gives 39 g s^{-1} . In ITER, the pedestal width is $\sim 8 \text{ cm}$, the warm-up time is $26 \mu\text{s}$ for maximum pellet speed 3 km s^{-1} if we use gyrotron pellet accelerator [25]. With a $B = 6 \text{ T}$ in ITER, a factor of ~ 3 reduction in ablation rate from the hydro simulation would be possible.

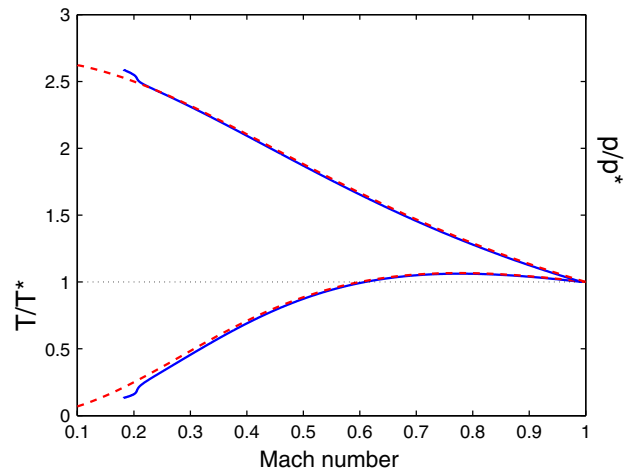


Figure 14. Normalized temperature and pressure in the ablation channel. The solid lines are from the simulation in 2 T magnetic field with electrostatic shielding, and the dashed lines are from the parallel flow model for the ablation channel [10].

We expect to improve the numerical algorithm by adding the adaptive mesh refinement. The low temperature region around the pellet will be discretized on a fine mesh, while the high temperature region of the ablation cloud and the ambient

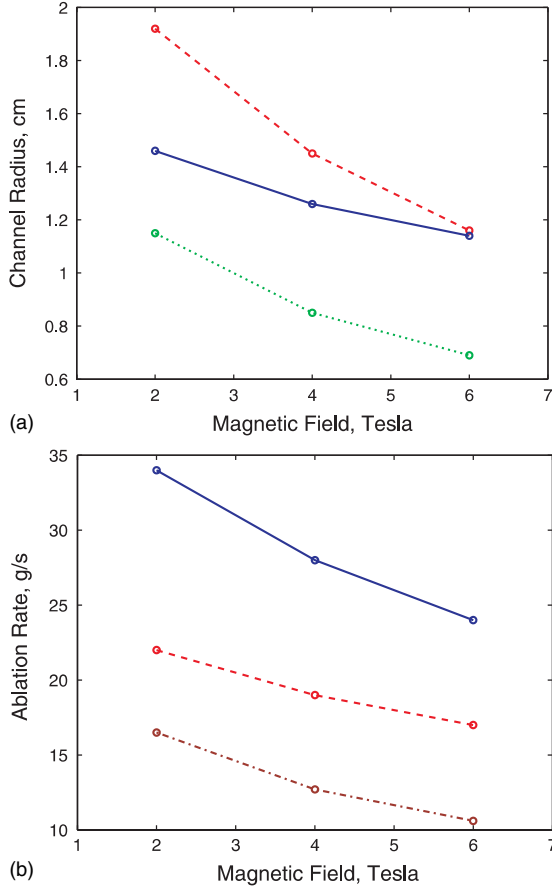


Figure 15. (a) Radius (cm) of the ablation channel as a function of the magnetic field strength, solid line for $10 \mu\text{s}$ warm-up time with $n_e = 10^{14} \text{ cm}^{-3}$, dashed line for $10 \mu\text{s}$ warm-up time with electrostatic shielding, and dotted line for $5 \mu\text{s}$ warm-up time with $n_e = 10^{14} \text{ cm}^{-3}$. (b) Ablation rate as a function of the magnetic field. The solid and dashed curves have the same parameters as the corresponding ones in (a), and the dash-dotted curve is obtained with $5 \mu\text{s}$ warm-up time with electrostatic shielding included.

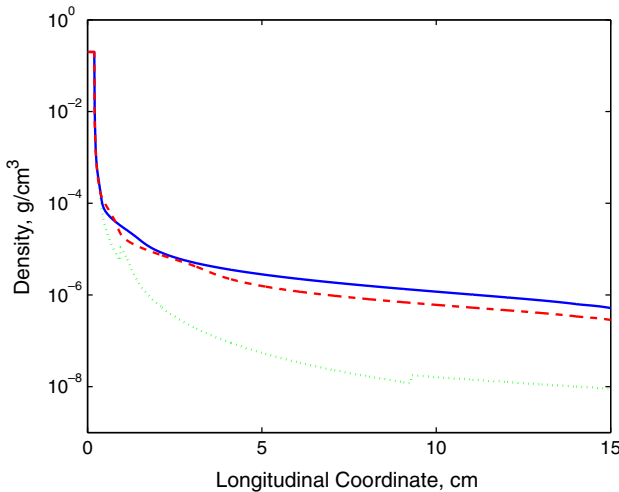


Figure 16. Density of the ablation cloud along the z -axis of the 1D spherically symmetric hydrodynamic model (dotted line), and 2D MHD models at $B = 6 \text{ T}$ with $n_e = 10^{14} \text{ cm}^{-3}$ (solid line) and $B = 2 \text{ T}$ with $n_e = 1.6 \times 10^{13} \text{ cm}^{-3}$ (dashed line).

Table 1. The ratio of the induced magnetic field to the toroidal magnetic field in the tokamak. Values near the pellet and far away from the pellet down the channel are calculated.

$n_e \setminus B$	2 T		4 T		6 T	
	δ_{near}	δ_{far}	δ_{near}	δ_{far}	δ_{near}	δ_{far}
10^{14} cm^{-3}	0.530	0.822	0.128	0.223	0.051	0.100
$1.6 \times 10^{13} \text{ cm}^{-3}$	0.110	0.180	0.029	0.055	0.015	0.026

plasma domains will contain much coarser grids, providing less limitation of the computational time step. This will allow us to simulate longer time intervals and increase the warm-up time. We will then calculate the MHD reductions of the ablation rate in low pellet velocity experiments and predict pellet ablation rates in ITER with more confidence using realistic distributions of the plasma temperature and density in the pedestal region. The other simplification, the effective shielding length, which was set to 15 cm in this work independently of the magnetic field, will also be improved in the future work by a self-consistent model.

In order to justify the low magnetic Reynolds number approximation of the MHD equations, we calculated the near-field and far-field inductance rate $|\Delta B/B|$, which are denoted by δ_{near} and δ_{far} , respectively, in table 1. The induced magnetic field near the pellet is calculated using the Biot–Savart law. Far from the pellet along the channel, the inertial term in momentum equation is considered to be small, and δ_{far} is half the magnetic β , which is the ratio of the channel pressure to the energy density of the magnetic field. The first row of table 1 lists cases of $n_e = 10^{14} \text{ cm}^{-3}$ and $T_e = 2 \text{ keV}$, the toroidal magnetic field ranging from 2 T to 6 T. If the electrostatic reduction of the electron heat flux is taken into account by using the electron density $n_e = 1.6 \times 10^{13} \text{ cm}^{-3}$, $|\Delta B/B|$ is further reduced as shown in the second row of table 1. Therefore, we conclude that Faraday’s Law is indeed negligible for realistic tokamak parameters.

5. Conclusions

A magnetohydrodynamic model for the study of the pellet ablation in 2D axisymmetric approximation has been developed based on the low magnetic Reynolds number approximation of the MHD system of equations and the method of front tracking. In the front tracking method, explicit interfaces separate the solid pellet from the ablated gas and the cold, dense and weakly ionized ablation cloud from the highly conducting fusion plasma. This allows the use of different mathematical and numerical approximations in complex geometrical domains occupied by different material substances, and thus the resolution of different material properties and time scales. The model has been validated through the comparison with theory and previous simulations. The 1D version of our model is in excellent agreement with the scaling laws and ablation rate predicted by the Transonic Flow model [3]. The 2D axisymmetric simulations of the ablation flow structure agree with results of MacAulay [8], and Ishizaki *et al* [9]. However, we show that the geometric effects (axisymmetric approximation) have a relatively minor

role in pure hydrodynamic models: the pellet ablation rate in the axisymmetric model was 0.82 of that in the spherically symmetric 1D model.

Pellet ablation rates and ablation flow properties in magnetic fields have been systematically studied in this paper for the first time. We have shown that the increase in the magnetic field reduces the ablation channel width and the pellet ablation rate. The main conclusion of the paper is that the directional channelling of the ablated material by the magnetic field leads to the redistribution of density and reduces the pellet ablation rate depending on the rise time of heat flux seen by the pellet. Shorter ‘warm-up’ times lead to narrower ablation channels, stronger shielding and reduced ablation rates. This new feature implies that pellets traversing strong plasma gradients, as in the edge pedestal region of the ITER plasma, could have significantly lower ablation rates if injected at higher velocity.

We have also determined that the low magnetic Reynolds number approximation is appropriate for realistic tokamak parameters. It is unsatisfactory at only very low magnetic fields and high densities of hot plasma electrons in the ablation cloud.

In the future, we will perform simulations using accurate distributions of the plasma density and temperature in the pedestal region and incorporate a channel rotation model due to the $\mathbf{E} \times \mathbf{B}$ force. The developed model is also a basis for the future study of striation instabilities and the pellet ablation in 3D.

Acknowledgments

This manuscript has been authored in part by Brookhaven Science Associates, LLC, under Contract No DE-AC02-98CH10886 with the US Department of Energy. The United States Government retains, and the publisher, by accepting the article for publication, acknowledges, a worldwide licence to publish or reproduce the published form of this manuscript, or allow others to do so, for the United States Government purpose. This research partially used resources of the National Energy Research Scientific Computing Center, which is supported by the Office of Science of the US Department of Energy under Contract No DE-AC03-76SF00098.

Appendix. Relation between exponents in Saha equations and plasma EOS

Given

$$PV = \left(\frac{1}{2} + \frac{f_d}{2} + f_i \right) RT,$$

$$E = \left(\frac{1 - f_d}{2(\gamma_m - 1)} + \frac{f_d + f_i}{\gamma - 1} \right) RT + \frac{1}{2} f_d R \epsilon_d + f_i R \epsilon_i,$$

$$\frac{f_d^2}{1 - f_d} = N_d V T^{\alpha_d} e^{-\epsilon_d/T},$$

$$\frac{f_i^2}{1 - f_i} = N_i V T^{\alpha_i} e^{-\epsilon_i/T}$$

with $\gamma = 5/3$, $R = k/m$, $V = 1/\rho$, we will prove that

$$\alpha_d = 3 - \frac{1}{\gamma_m - 1},$$

$$\alpha_i = \frac{3}{2}.$$

Proof. The second law of thermodynamics requires that $TdS = dE + PdV$, and therefore

$$dS = \frac{dE}{T} + \frac{P}{T} dV = \frac{1}{T} \left. \frac{\partial E}{\partial T} \right|_V dT + \frac{1}{T} \left(\left. \frac{\partial E}{\partial V} \right|_T + P \right) dV, \quad (19)$$

from which we have

$$\frac{\partial}{\partial V} \left(\frac{1}{T} \left. \frac{\partial E}{\partial T} \right|_V \right) = \frac{\partial}{\partial T} \left(\frac{1}{T} \left(\left. \frac{\partial E}{\partial V} \right|_T + P \right) \right), \quad (20)$$

which reduces to

$$T \left. \frac{\partial P}{\partial T} \right|_V - P = \left. \frac{\partial E}{\partial V} \right|_T. \quad (21)$$

Using the plasma EOS, the left-hand side of equation (21) is

$$T \left. \frac{\partial P}{\partial T} \right|_V - P = \frac{RT^2}{V} \left. \frac{\partial}{\partial T} \right|_V \left(\frac{1}{2} + \frac{f_d}{2} + f_i \right)$$

$$= \frac{RT^2}{V} \left[\frac{1}{2} \left. \frac{\partial f_d}{\partial T} \right|_V + \left. \frac{\partial f_i}{\partial T} \right|_V \right]. \quad (22)$$

The right-hand side is

$$\left. \frac{\partial E}{\partial V} \right|_T = \left[\left(-\frac{1}{2(\gamma_m - 1)} + \frac{1}{\gamma - 1} \right) RT + \frac{1}{2} R \epsilon_d \right] \left. \frac{\partial f_d}{\partial V} \right|_T$$

$$+ \left[\frac{1}{\gamma - 1} RT + R \epsilon_i \right] \left. \frac{\partial f_i}{\partial V} \right|_T. \quad (23)$$

Comparing equation (22) and equation (23), we obtain

$$\frac{RT^2}{V} \frac{1}{2} \left. \frac{\partial f_d}{\partial T} \right|_V = \left[\left(-\frac{1}{2(\gamma_m - 1)} + \frac{1}{\gamma - 1} \right) RT + \frac{1}{2} R \epsilon_d \right] \left. \frac{\partial f_d}{\partial V} \right|_T,$$

$$\frac{RT^2}{V} \left. \frac{\partial f_i}{\partial T} \right|_V = \left[\frac{1}{\gamma - 1} RT + R \epsilon_i \right] \left. \frac{\partial f_i}{\partial V} \right|_T. \quad (24)$$

$$\frac{RT^2}{V} \left. \frac{\partial f_i}{\partial T} \right|_V = \left[\frac{1}{\gamma - 1} RT + R \epsilon_i \right] \left. \frac{\partial f_i}{\partial V} \right|_T. \quad (25)$$

On the other hand, from the two Saha equations we have the following relations between the derivatives:

$$\frac{1}{V} \left. \frac{\partial f_d}{\partial T} \right|_V = \left(\frac{\alpha_d}{T} + \frac{\epsilon_d}{T^2} \right) \left. \frac{\partial f_d}{\partial V} \right|_T, \quad (26)$$

$$\frac{1}{V} \left. \frac{\partial f_i}{\partial T} \right|_V = \left(\frac{\alpha_i}{T} + \frac{\epsilon_i}{T^2} \right) \left. \frac{\partial f_i}{\partial V} \right|_T. \quad (27)$$

Comparing equation (25) and equation (27), it is straightforward to show that

$$\alpha_i = \frac{1}{\gamma - 1}.$$

Since $\gamma = 5/3$, $\alpha_i = 3/2$. Similarly, comparing equation (24) and equation (26) we can obtain that

$$\alpha_d = \frac{2}{\gamma - 1} - \frac{1}{\gamma_m - 1}.$$

For $\gamma = 5/3$, $\alpha_d = 3 - 1/(\gamma_m - 1)$.

References

- [1] Davis J.W. and Kulcinski G.L. 1976 *Nucl. Fusion* **16** 355
- [2] ITER Physics Expert Group on Divertors F.W. Perkins, D.E. Post, N.A. Uckan *et al* (ed) 1999 Power and particle control (chapter 4) *Nucl. Fusion* **39** 2391
- [3] Parks P.B. and Turnbull R.J. 1978 *Phys. Fluids* **21** 1735
- [4] Felber F.S., Parks P.B., Prater R. and Vlasov D.F. 1979 *Nucl. Fusion* **19** 1061
- [5] Parks P.B. 1980 *Nucl. Fusion* **20** 311
- [6] Kuteev B.V. *et al* 1985 *Sov. J. Plasma Phys.* **11** 236
- [7] Parks P.B. and Rosenbluth M.N. 1998 *Phys. Plasmas* **5** 1380
- [8] MacAulay A.K. 1994 *Nucl. Fusion* **34** 43
- [9] Ishizaki R., Parks P.B., Nakajima N. and Okamoto M. 2004 *Phys. Plasmas* **11** 4064
- [10] Parks P.B., Sessions W.D. and Baylor L.R. 2000 *Phys. Plasmas* **5** 1968
- [11] Samtaney R., Jardin S., Colella P. and Martin D. 2003 *Princeton Plasma Physics Laboratory Report PPPL-3891*
- [12] Parks P.B. and Baylor L.R. 2005 *Phys. Rev. Lett.* **94** 125002
- [13] Samulyak R. and Prykarpatsky Y. 2004 *Mathe. Comput. Simul.* **65** 431
- [14] Glimm J., Grove J.W., Li X.L., Shyue K.L., Zhang Q. and Zeng Y. 1998 *SIAM J. Sci. Comput.* **19** 703
- [15] Parks P.B. 1996 *Plasma Phys. Control. Fusion* **38** 571
- [16] Zel'dovich Y.B. and Raizer Y.P. 1966 *Physics of Shock Waves and High-Temperature Hydrodynamic Phenomena* vol I (New York: Academic)
- [17] Glimm J., Grove J. and Zhang Y. 2002 *SIAM J. Sci. Comput.* **24** 208
- [18] Menikoff R. and Plohr B. 1989 *Rev. Mod. Phys.* **61** 75
- [19] Glimm J., Grove J.W., Li X.L. and Tan D.C. 2000 *SIAM J. Sci. Comput.* **21** 2240
- [20] Colella P. and Woodward P. 1984 *J. Comput. Phys.* **54** 174
- [21] van Leer B. 1979 *J. Comput. Phys.* **32** 101
- [22] Parks P.B. 1992 *Nucl. Fusion* **32** 2137
- [23] Veselova I.Yu. and Rozhansky V.A. 1991 *Sov. J. Plasma Phys.* **17** 817
- [24] Parks P.B. 1991 *Nucl. Fusion* **31** 1431
- [25] Parks P.B. and Perkins F.W. 2006 *Nucl. Fusion* **46** 770